Characterization of Pore Defects and Fatigue Cracks in Die Cast AM60 Using 3D X-ray Computed Tomography

ZHUOFEI YANG, JIDONG KANG, and DAVID S. WILKINSON

AM60 high pressure die castings have been used in automobile applications to reduce the weight of vehicles. However, the pore defects that are inherent in die casting may negatively affect mechanical properties, especially the fatigue properties. Here we have studied damage (*e.g.*, pore defects, fatigue cracks) during strained-controlled fatigue using 3-dimensional X-ray computed tomography (XCT). The fatigue test was interrupted every 2000 cycles and the specimen was removed to be scanned using a desktop micro-CT system. XCT reveals pore defects, cracks, and fracture surfaces. The results show that pores can be accurately measured and modeled in 3D. Defect bands are found to be made of pores under 50 μm (based on volume-equivalent sphere diameter). Larger pores are randomly distributed in the region between the defect bands. Observation of fatigue cracks by XCT is performed in three ways such that the 3D model gives the best illustration of crack–porosity interaction while the other two methods, with the cracks being viewed on transverse or longitudinal cross sections, have better detectability on crack initiation and crack tip observation. XCT is also of value in failure analysis on fracture surfaces. By assessing XCT data during fatigue testing and observing fracture surfaces on a 3D model, a better understanding on the crack initiation, crack–porosity interaction, and the morphology of fracture surface is achieved.

I. INTRODUCTION

MAGNESIUM alloys are attractive to the automotive industry as they are lighter than aluminum in weight and have good castability. The use of magnesium alloy components in new generation light weight vehicles will improve fuel economy. High pressure die casting (HPDC) is cost-effective, producing large volume magnesium casting components in net shape and with complex geometry.[1] However, the inherent porosity of the casting process retards their wider use. The porosity issue is more serious in thick-wall than thin-wall castings;[1] the former offers a cross section with two microstructures, fine-grain pore-free surface microstructure and coarse-grain internal microstructure with pores. Porosity usually involves both gas pores and shrinkage pores. The former result from the gas entrapment during the rapid injection of molten metal into the die cavity while the latter are due to the volumetric contraction of solidified metal and the lack of extra molten metal to refill the die cavity.

The presence of porosity in a magnesium casting impairs its mechanical performance, especially fatigue properties. Several studies of the fatigue properties of AM60 Mg castings have been conducted.[2,3] The scatter of pore size in AM60 die casting was concluded to be the dominant factor resulting in the large scatter of fatigue life in stress-controlled fatigue.[2] In strain-controlled fatigue, the scatter of fatigue life was also found to be large at low strain levels.[3] The size measurements of porosity in 2D on cross sections or fracture surfaces are not accurate since pores are 3D objects. Therefore, a further in-depth study on the effect of porosity on fatigue properties of AM60 HPDC Mg alloy using X-ray computed tomography (XCT) technique to characterize porosity in 3D will better reveal the role of porosity in fatigue behavior. By conducting an interrupted fatigue test and XCT scan on a specimen at intervals, the effect of porosity on both the crack initiation and crack propagation stages can be studied. Even the fracture surfaces after fatigue testing can be 3D determined by XCT to facilitate failure analysis when interpreted by SEM images. Not only the size of porosity will be measured more accurately in 3D, but also the shape and the location. The interaction of fatigue cracks and porosity during fatigue test can also be visualized.

XCT has been increasingly used in material science as a non-destructive tool to visualize and characterize the internal structure of materials. By reconstructing data from a large number of 2D projection images taken during the XCT scan, through-thickness cross-sectional

ZHUOFEI YANG, Graduate Student, is with the Department of Materials Science and Engineering, McMaster University, Hamilton, L8S 4L8, Canada, and also with CanmetMATERIALS, Natural Resources Canada, Hamilton L8P 0A5, Canada. JIDONG KANG, Research Scientist, is with the Department of Natural Resources, CanmetMATERIALS. Contact e-mail: jkang@nrcan.gc.ca DAVID S. WILKINSON, Distinguished University Professor, Provost & Vice President (Academic), is with the Department of Materials Science and Engineering, McMaster University.

images can be obtained and a 3D model can be developed. Detectability and resolution is much better than conventional X-ray radiography and ultrasound. In recent years XCT has been transformed from simple qualitative observation to quantitative analysis. From XCT scanning, 3D objects (*e.g.*, pore defects and cracks) could be quantitatively characterized. Compared with large-scale synchrotron X-ray sources, laboratory X-ray source tomography is about two orders of magnitude slower.[4] However, this is offset by the greater availability of the technique. Several papers have shown how the XCT technique can be used in fatigue property studies[5–9] with respect to porosity measurements and recording fatigue crack evolution. Therefore, a study using XCT throughout the fatigue test, including post-test analysis, is of interest. It will help us understand further the capability of XCT in fatigue property study. This research was focused on the use of XCT to record fatigue crack evolution and the interaction of cracks with porosity. The objectives of this research are, first, to verify the key parameters extracted using XCT analysis, such as 3D measurements of porosity; second, to detect and visualize the fatigue crack initiation and propagation during the fatigue test; and third, to examine the value of XCT scan data in assessing failure analysis from SEM observation.

II. EXPERIMENTAL

The HPDC Mg alloy AM60 used in the current study was provided by CanmetMATERIALS, in form of a shock tower. The chemical composition is given in Table I. Specimens were extracted from six locations within the shock tower as shown in Figure 1. They all had the same thickness of 3mm. Specimens used in current research work were prepared by electro-discharge machining (EDM) on the edges and the top and bottom casting surfaces were reserved as the original casting surface, as shown in Figure 2.

In this paper we report on interrupted fatigue tests conducted on two specimens extracted from location No. 1 and No. 2, respectively. The tests were performed at room temperature under strain control at 0.3 pct strain amplitude, with a strain ratio $R = -1$ and frequency of 0.5 Hz. A 3-mm extensometer was attached to the specimen to measure the longitudinal strain. Fatigue tests were interrupted every 2000 cycles and the specimen was removed for XCT.

To compare the fatigue results of the current study with the work of Rettberg *et al.*[3] in which different dimensions of specimens and an extensometer of a different length was used, a finite element (FE) simulation was conducted using ABAQUS (version 6.13) to determine the local strain in the center of the specimen

at different global strain levels read from the extensometer. 3D brick elements of C3D8R were used to mesh 1/8th of the specimen geometry, taking advantage of the X, Y, and Z symmetries. An elastic–plastic model with isotropic hardening was generated using the tensile-test stress–strain data. The displacement at the ends of the extensometer location and the true strain in the center were tracked.

X-ray tomography and radiography was performed using a Skyscan 1172 high-resolution micro-CT scanner. The projection images taken during XCT scan at different angles were reconstructed using "NRecon" software to obtain tomography images showing cross sections of the specimen. Subsequently, the "CT-Analyser" and "CT-Volume" programs were used for 2D/3D quantitative analysis and 3D visualization, respectively. The XCT scan was performed on fatigue specimens prior to, during, and after fatigue tests to record the evolution of porosity and fatigue cracking. A scan of the fatigue specimen before each test was obtained to capture the initial internal porosity. A final scan following the test was used to construct a 3D model of the fractured specimen and observe fracture surfaces in order to assist the failure analysis by SEM observation. Radiography images were used to compare with 3D model.

The details of the XCT scan parameters are as follows. The X-ray source operates at a voltage of 65 kV. The scanning volume covers a 10-mm length in the center of specimen. The X-ray source, the fatigue specimen, and the CCD camera were positioned on a straight line, with specimen in the center. During each scan, the specimen was rotated through 360 deg with a step of 0.7 deg. The CCD camera, in "large camera" mode, provided 1000*668 resolution images to form 2D projection images at each step. The pixel size is 6.05 μm, giving a voxel size of 221.4 μm^3. A 0.5-mm Al filter is used.

The microstructure of fatigue specimen cross section was observed before fatigue test and SEM was used for fractography analysis.

III. RESULTS AND DISCUSSION

A. *Optical Microscope Observation*

The as-polished microstructure of the cross section is shown in Figure 3. The sample for microstructure observation was cut from the grip section of fatigue test specimens. The bottom of the cross section in Figure 3(a) indicates the existence of a pore-free casting surface microstructure. At about 400 μm below the casting skin surface, a defect band was observed consisting of tiny irregular-shaped porosity. Large pores

Table I. Chemical Composition of the AM60B Alloy in Weight Percent

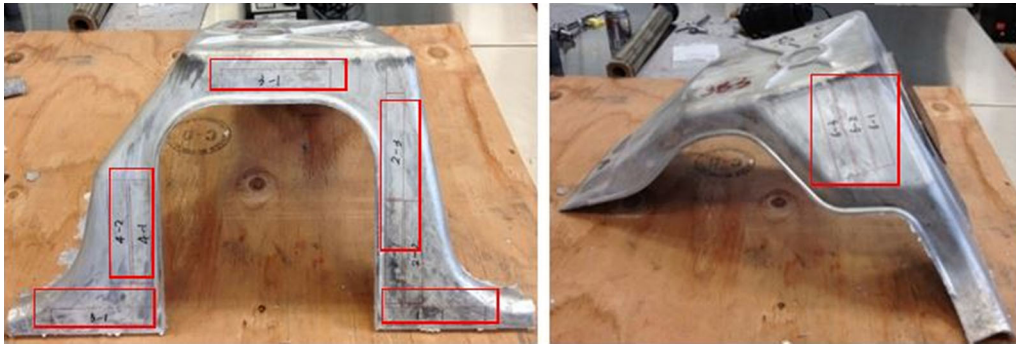| Mg	Al	Mn	Si	Zn	Sn	Pb	Fe	Cu	Ni	Be
Bal.	6.0	0.37	<0.01	<0.01	<0.01	<0.01	0.003	<0.001	<0.001	<0.001

Fig. 1—Photographs of AM60 shock tower; six locations for extracting specimens are marked.
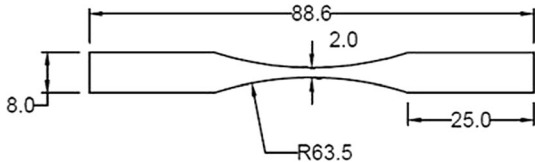

Fig. 2—Dimension of fatigue test specimen; all dimensions are in mm.

were found in the center area of the thickness surrounded by small shrinkage pores.

B. Fatigue Test Result

Two specimens were used for interrupted fatigue testing and the results were plotted along with the results from Rettberg et al.[3] The FE simulation results show how the local strain vs global strain differs for the two kinds of specimen geometry. The results are plotted in Figure 4. Both specimen geometries show a local strain in the center higher than the global strain measured by the extensometer, especially for the specimen geometry used in the study of Rettberg et al.[3] The discrepancy between global strain and the corresponding local strain is listed in Table II. In the current study, the global strain read from a 3-mm extensometer predicted the local strain in the center rather well; the local strain corresponding to the global strain of 0.3 is 0.33 pct. Therefore, instead of using the strain read from an extensometer, the local strain in the center was plotted vs the fatigue life in Figure 5. Based on this comparison our results seem to follow the same trend as those of Rettburg et al.[3] In the current experiment, specimen No. 1 showed a crack detected by XCT after 2478 cycles; further fatigue testing was not conducted. Specimen No. 2 was fatigue tested until 6000 cycles with the first crack detection done after 5784 cycles.

C. X-ray Tomography and Radiography on Porosity

Two 3D models of the scanned volume were developed to show the internal porosity as shown in Figure 6. In this model, the AM60 Mg alloy matrix was set transparent to reveal porosity. To effectively reduce the noise produced in the reconstruction process, pores smaller than eight voxels in volume, equivalent to 15 μm
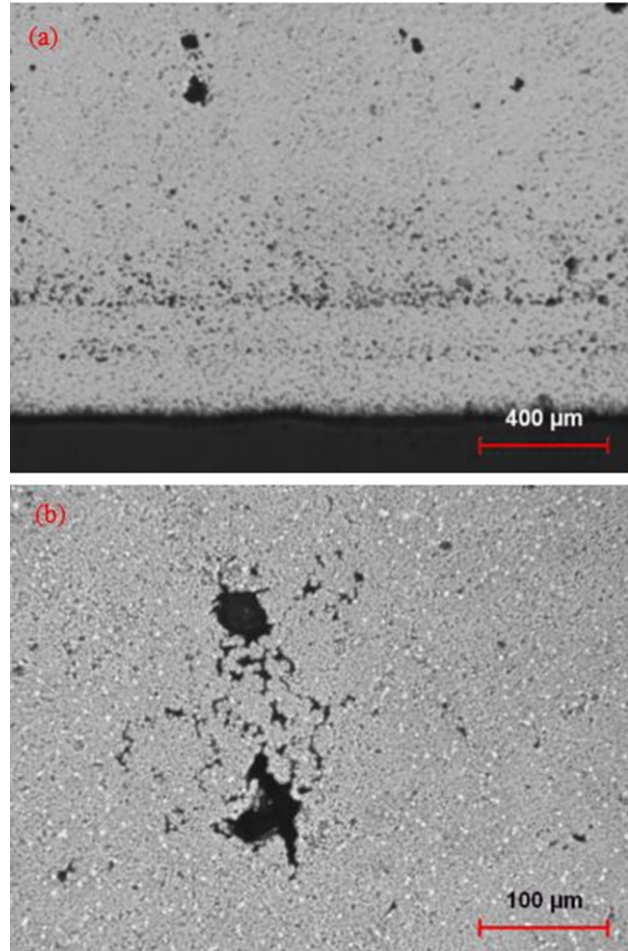

Fig. 3—Optical micrographs show (a) distribution of pores through-thickness and (b) large pores in the interior.

in volume-equivalent sphere diameter, were removed. The volume-equivalent sphere diameter is used here to describe the pore size. It is extracted from the 3D analysis and defined as the diameter of a sphere which has same volume as the pore being studied. Different colors were assigned to the pore population to distinguish their sizes.

Pores less than 50 μm in diameter, were found to make up the majority of the pore population. Specimen
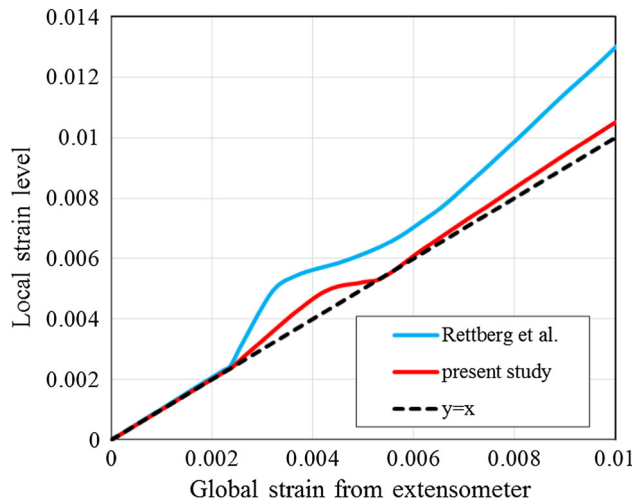
Fig. 4—The local strain amplitude in the center of the specimen for two sets of dimensions simulated by ABAQUS.

Fig. 5—Strain *vs* fatigue life from the study of Rettberg *et al.* [3] and the current data.

Table II.   The Extensometer Strain and the Corresponding Strain at the Center in the Specimens of Rettberg *et al.*[3]

Extensometer Strain (pct)	Strain at the Center (pct)
0.20	0.20
0.40	0.57
0.60	0.70
0.80	1.00
1.00	1.30

No. 1 was observed to contain a larger scatter of pore size than specimen No. 2. The largest pore in specimen No. 2 is in the range of 200 to 300 μm in diameter (green) while specimen No. 1 has pores 300 to 400 μm in size (yellow). In addition, specimen No. 1 had a number of large surface pores while for specimen No. 2, the number and size of surface pores are too small to be counted. Compared with the 3D model showing porosity, radiography only shows several blurred dots in a light gray color. They correspond to the surface voids and some of the large internal pores shown in Figure 6(a). XCT is clearly superior for detecting porosity than radiography.

Defect bands were found to be made of pores under 50 μm in diameter. A 3D model cross-sectional image of specimen No. 2, cut along the loading direction and perpendicular to the casting surfaces, shows that most of the pores under 50 μm are located in a defect band region and only a few are located in the region between the defects bands. The region outside the defect bands represents the casting skin surface region with a small amount of microporosity. In addition, the largest pores in specimen No. 2 were found in the defect band region.

The other pores with larger size were found to be distributed uniformly in the internal region (between the two casting skin surfaces), thus indicating that larger pores were formed during the solidification process. They have been interpreted as artificial pores resulting from degassing during the solidification process.[5] The small sphericity feature measured for large pores indi-
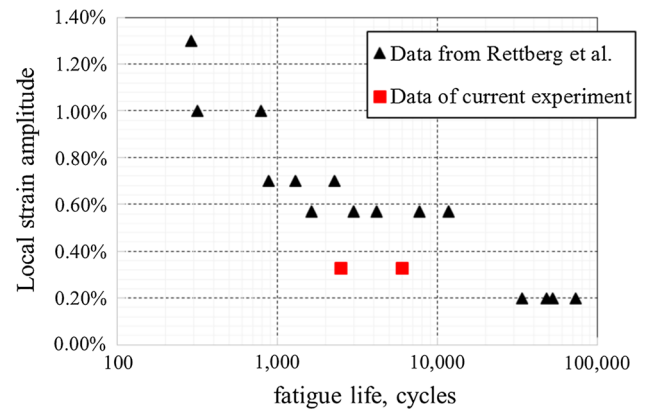
cates that solidified dendrites hindered the growth of the pore and resulted in an irregular shape.[5]

Reconstructed tomography images were used to extract key parameters of porosity. The number of pores in the scanned volume, as well as the volume and the shape of individual pores were determined.

Specimen No. 1 was found to contain 35,231 pores in the scanned volume with a volume fraction of porosity of 2.31 pct, of which 1.29 pct represents surface voids and 1.02 pct internal pores. Specimen No. 2 has 22,232 pores and porosity takes up 0.40 pct of volume. The pores under 50 μm in diameter respectively take up 94.8 and 98.1 pct of total porosity population in these two specimens.

A statistical analysis considering volume is shown in Figure 7. The internal pores were grouped into five sets according to their size and the percentage of each group making up the total porosity volume is calculated. It was found that in specimen No. 2 the majority of the pore volume, 63.8 pct, is contributed by pores ranging in size from 15 to 50 μm in diameter while for other (larger) pore ranges the percentages are all smaller than the corresponding values in specimen No. 1. Therefore specimen No. 1 is characterized as having a larger amount of porosity, a larger scatter of pore size, and a larger average pore size.

D. *X-ray Tomography and Radiography on Crack*

The fatigue cracks and their interaction with porosity in both specimens are shown below while the evolution of fatigue cracks was only followed in specimen No. 2. XCT analysis provides three ways to observe cracks, either in 3D or 2D.

1. *Crack observation in the 3D model*

Since porosity and cracks are just two forms of empty space within a specimen, the attenuation of the X-ray beam for each of them is same, which means they cannot be distinguished when binarizing tomography images for the 3D model, *i.e.*, they appear as the same color in the 3D model. The 3D models showing cracks and some
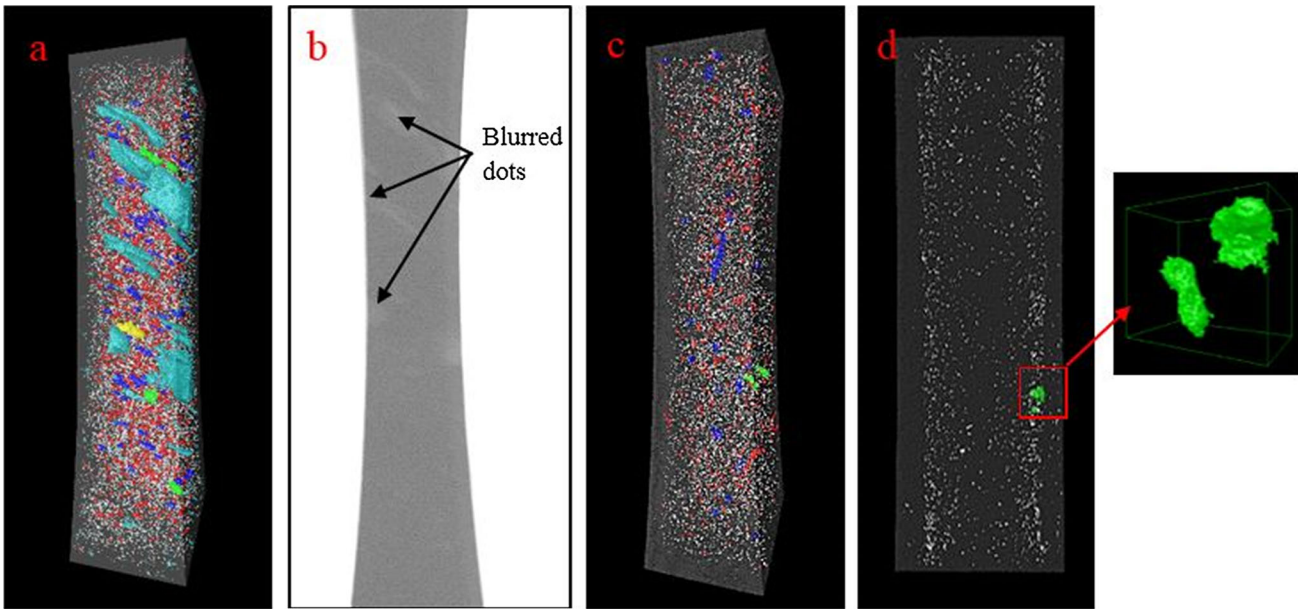
Fig. 6—(*a*) 3D model of specimen No. 1, (*b*) radiography image of specimen No. 1, (*c*) 3D model of specimen No. 2, and (*d*) a longitudinal cross-sectional image of specimen No. 2. White porosity is less than 50 *μ*m in diameter: red is in the range of 50 to 100 *μ*m, blue is 100 to 200 *μ*m, green is 200 to 300 *μ*m, yellow is 300 to 400 *μ*m, and light blue is for surface voids (Color figure online).
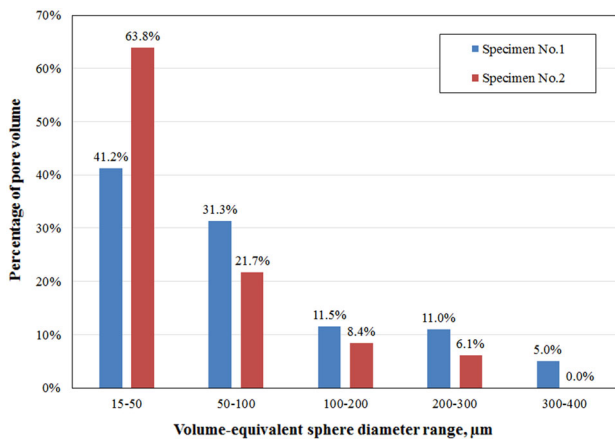
Fig. 7—Percentage of porosity volume in each group taking up total porosity volume.

pores in different colors were produced by comparing two separate 3D models. In Figures 8 and 9, the voids associated with cracks were subtracted from the 3D model of the initial data of porosity taken before fatigue test thus enabling us to distinguish cracks and pores that are developed during the fatigue test.

In specimen No. 1 the fatigue crack initiated from a void on the machined surface. It can be observed in Figure 8(b) that the crack was initiated on both sides of the surface pore and the crack propagation is faster on the left side than the right. On the left side, the crack shown in Figure 8(a) was flat at first; then the crack path changed in the vicinity of the casting surface. It was previously seen by optical microscopy (Figure 3(a)) that a defect band starts at 400 *μ*m from casting surface. Therefore, the change of crack path in specimen No. 1 is believed to have happened in the defect band region.
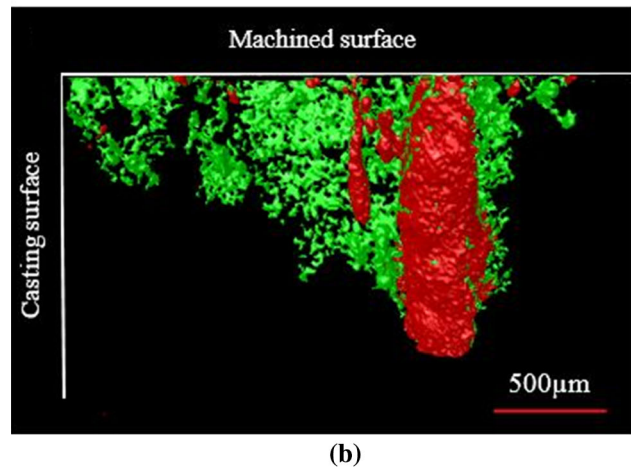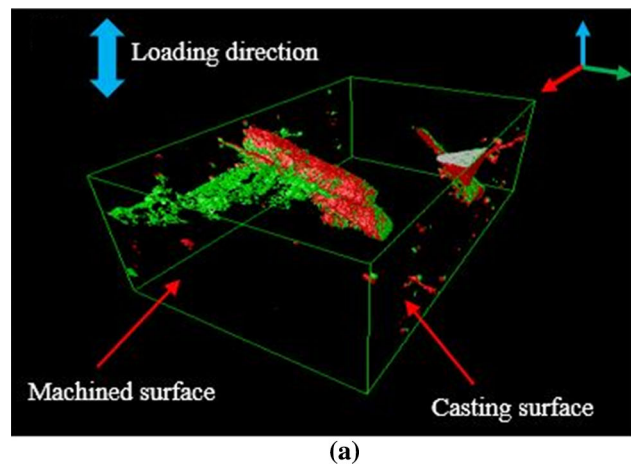

Fig. 8—(*a*) 3D model of the specimen No. 1 in the center region after 2478 cycles and (*b*) top view of crack and associated surface void; green color is crack and red is porosity (Color figure online).
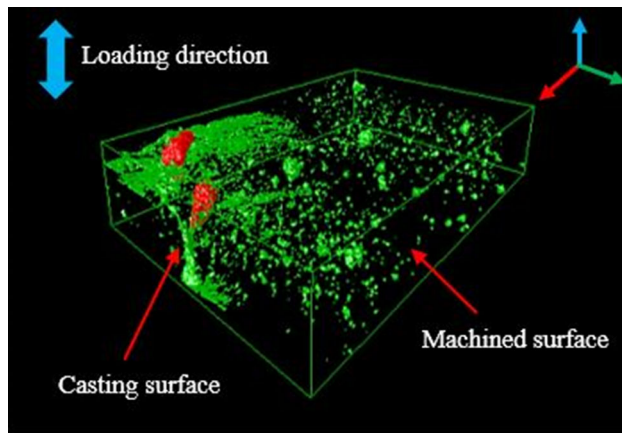
Fig. 9—3D model of a section of specimen No. 2.

Three cracks were observed from different initiation sites and height levels in specimen No. 2 after 6000 cycles, as shown in Figure 9. The red pores, being the largest pores in specimen No. 2, were observed to initiate cracks while the pore just underneath the casting surface initiated the third crack.

The evolution of cracks in specimen No. 2 during the fatigue test is shown in Figure 10. Images are the top view of the 3D model in Figure 9 and represent different numbers of cycles during the fatigue test. Only the corner where cracks are located is shown. Two casting pores were partially overlapped from this perspective, but it is still obvious that cracks had initiated from the casting pores within 5784 cycles in Figure 10(c). Compared with Figures 10(a) and (b), the increase of green dots in number around the largest casting pores indicates that the crack was initiated from casting pores and then propagated in all directions. The crack initiated from the pore No. 1 mainly propagated in the through-thickness direction while the crack initiated from pore No. 2 was observed to propagate in the width direction through defect band region. The crack initiated from pore No. 3 propagated in a through-thickness direction.

One problem with observing crack evolution in the 3D model is that a part of the crack front may not be completely shown in 3D due to a failure to separate them from the matrix during the image binarizing process as their grayscales are too close to be distinguished. The tomography images in grayscales have to be binarized into black and white to create a 3D presentation of porosity and cracks. After binarizing, the black means pores or cracks and white is matrix. However, it is hard to completely recognize the crack front during the binarizing process as the grayscale of the crack front is close to that of the matrix. This lies in the fact that cracks are planar defects and there is crack closure upon unloading. Thus, the crack may not show a sufficient difference in grayscale to be distinguished from that of the matrix. As a consequence, the parts of the crack which are very thin, such as the crack front, can be misrecognized to be matrix material. In other words, the crack illustrated in the 3D model is the majority of a real crack that is thick enough to be identified as void space.

As outlined below, we have taken two approaches to addressing this concern.

2. Crack observation on tomography images

The 3D image of the crack is calculated from a series of XCT scans or slices through the sample. The cracks are generally oriented in a direction normal to the loading direction. Therefore slices of the 3D image across the sample (*i.e.*, perpendicular to the crack direction) can show a cross section of the crack on the corresponding tomography image in the form of a darker gray shadow. Cracks and porosity should present the same grayscale contrast on the tomography image. However, by considering the size and shape of a crack, it is understood that the slight difference in grayscales between crack and porosity is attributed to the zigzag shape of the crack, being a planar defect, and to the crack closure effect.

The crack evolution in specimen No. 2 is shown in Figure 11 by a series of tomography images obtained at different cycles. Before 4000 cycles, the crack is not visible on the tomography images while at 5784 cycles, a crack is seen that had initiated from the casting pore; the shadow surrounding the casting pore is the cross section of the crack on this tomographic slice. The crack shadow at 6000 cycles indicates that the crack initiated from the casting pore has propagated quickly in both the through-thickness and width direction. The reason why thin parts of the crack can be better observed in these images is that the spacing of two adjacent tomography images is 6 μm in this study. Therefore, any parts of the crack thicker than 6 μm will present a difference in grayscale between tomography images.

A similar observation of crack and porosity is shown in Figure 12. Cracks were observed to be initiated from two casting pores, corresponding to pore No. 1 and No. 2 in Figure 10(a). The crack initiated from pore No. 1 propagated in two directions; toward the machined surface and toward the interior. The latter was perpendicular to the loading direction in the early stage, and then gradually declined to connect with the crack initiated from pore No. 2. The crack initiated from pore No. 2 only propagated in one direction, through the width. The cracks shown at 6000 cycles are thicker and easier to identify. Compared with the crack from pore No. 2 shown in Figure 10, the corresponding crack shown in Figure 12(d) has propagated further into specimen.

3. Comparison of the crack observation with and without using a tensile fixture

After the fatigue crack has initiated, the two opposing faces of a fatigue crack could physically contact at the crack tip when unloaded, often referred to as the crack closure phenomenon.[10,11] This leads to a further underestimation of crack propagation so that the detection of XCT on the crack will be inaccurate due to insufficient pixel occupation on the crack. Therefore, a tensile fixture aiming to overcome crack tip closure was used to facilitate the detection of cracks by XCT. Specimen No. 1, in which a crack was detected after 2478 cycles, was scanned both in an as-unloaded
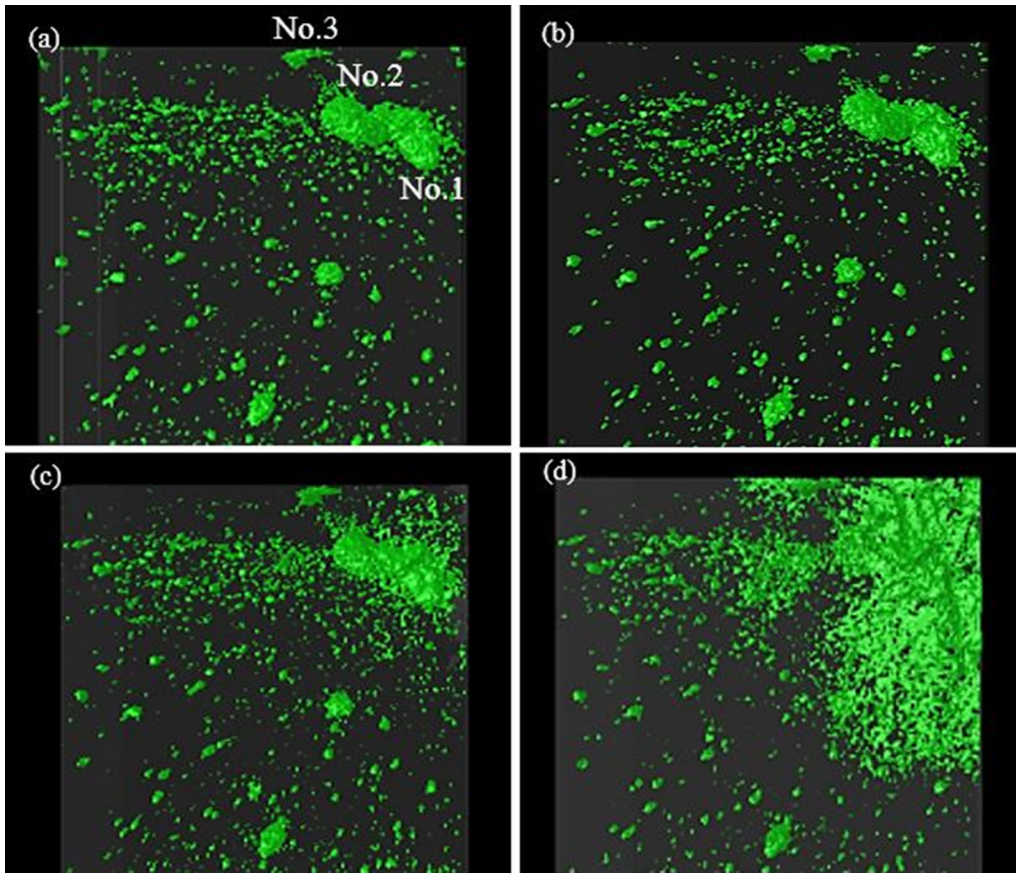
Fig. 10—Top view image of a 3D model of specimen No. 1 after (*a*) initial state, (*b*) 4000 cycles, (*c*) 5784 cycles, and (*d*) 6000 cycles. Three pores served as crack initiation sites, marked in (a). Loading direction is perpendicular to the images.
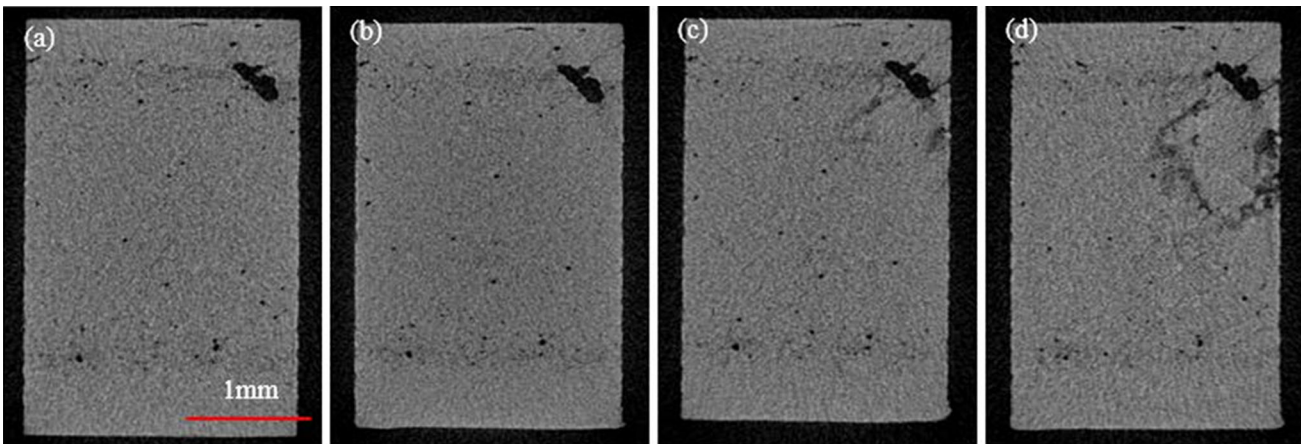

Fig. 11—The appearance of a tomography image during fatigue test in specimen No. 2 at (*a*) initial state, (*b*) 4000 cycles, (*c*) 5784 cycles, and (*d*) 6000 cycles. The darker gray shadow around the pore is the cross section of the fatigue crack represented on this tomography image. The loading direction is normal to the tomography images.

condition and under tension. In Figure 13, the same crack as in Figure 8(b) was overlaid with itself, having been scanned while under tension. The crack had actually propagated further on the lateral sides although the crack length was similar before and after applying tension. Figure 14 shows the comparison of crack thickness on longitudinal cross sections where the fatigue crack was found effectively pulled to open. As seen in Figure 14, by applying a tensile force the crack tip closure phenomenon could be eliminated during the XCT scan, ensuring that the XCT accurately detects and measures crack dimensions.
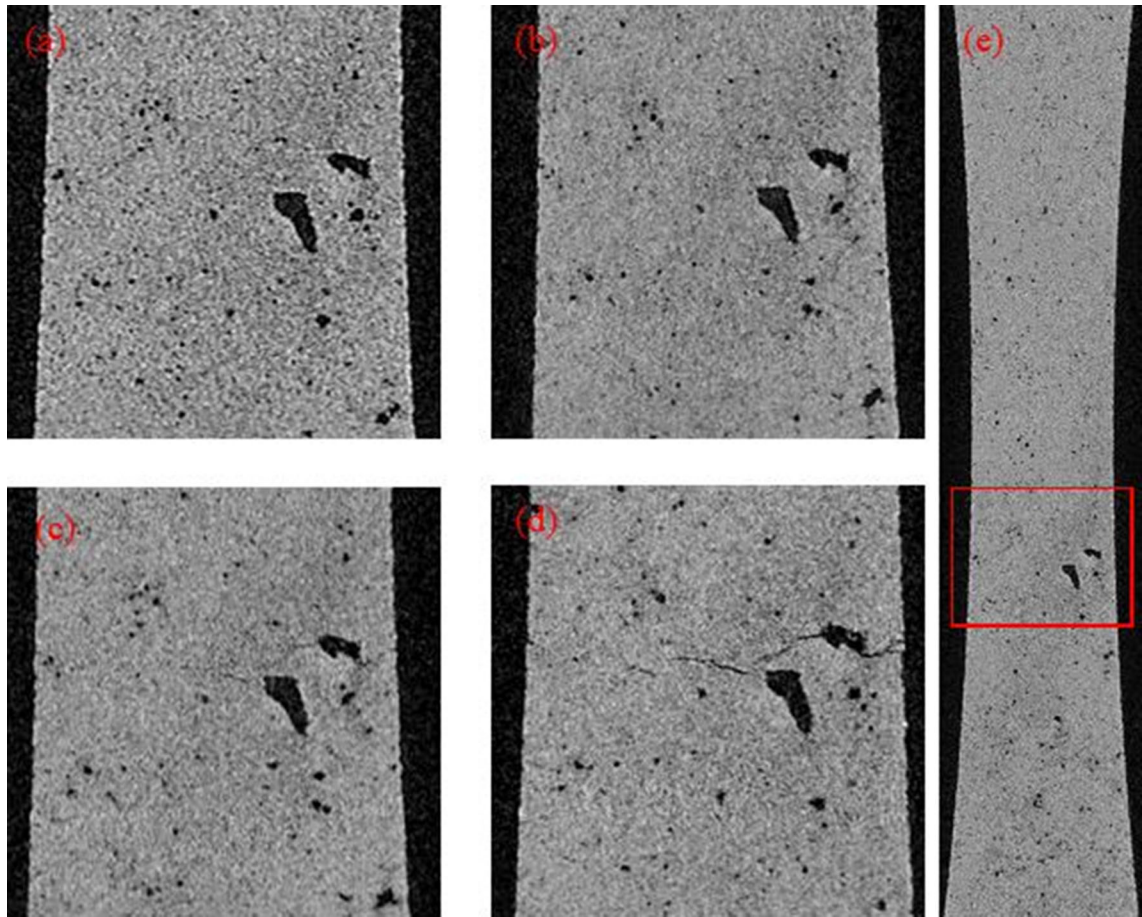
Fig. 12—Appearance of one resliced tomography image in specimen No. 2 at (*a*) initial state, (*b*) 4000 cycles, (*c*) 5784 cycles, (*d*) 6000 cycles, and (*e*) the overall view of initial state. The loading direction is vertical.
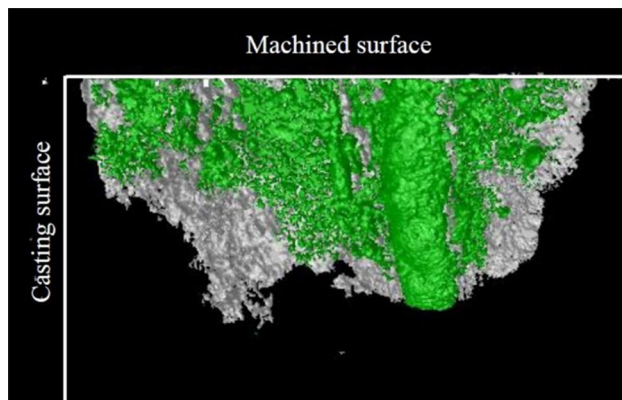

Fig. 13—Comparison of the crack shape with and without use of the tensile fixture in specimen #1; the green is when specimen is unloaded during XCT scan and the gray is specimen is elastically loaded during XCT scan. Loading direction is perpendicular to the image.

E. *Fractography Observation*

The fractography observation of specimen No. 2 was completed using both SEM and the 3D model. In Figure 15, a comparison of the overall fracture surface

between these two approaches suggests that the 3D model provides a more accurate morphology of the fracture surface. Figure 16 shows SEM images of the fatigue crack initiation sites on the fracture surface in relation to 3D XCT of pores observed in the specimens (*e.g.*, in Figure 10). The green and blue objects are illustrated in 3D, corresponding to the pores numbered in Figure 10: the green object is the pore No. 1 and the pore No. 2; the blue object is the pore No. 3. Two of three pores which served as crack initiation sites observed in X-ray tomography images and the 3D model, were observed in SEM while pore No. 2 is hiding under the fracture surface. Three crack paths were shown in Figure 16(b) and it is known from previous observation of the 3D model in Figure 9 that the crack path in the middle is from the pore No. 2 and the crack paths at the bottom and at the top are from pore No. 3 and pore No. 1, respectively.

The effect of porosity on crack initiation as well as the crack initiation sites were observed by XCT scans during the fatigue test. A post-test scan gives a better understanding of the fracture surface morphology. However, it cannot provide detailed information such as crack propagation modes or the striation pattern due to limited resolution.

IV. CONCLUSIONS

We used XCT to characterize pore defects and fatigue cracks during fatigue testing of an AM60 HPDC magnesium alloy. The use of XCT enables the characterization of internal defect structures and facilitates the failure analysis by SEM. The major findings are summarized as follows:
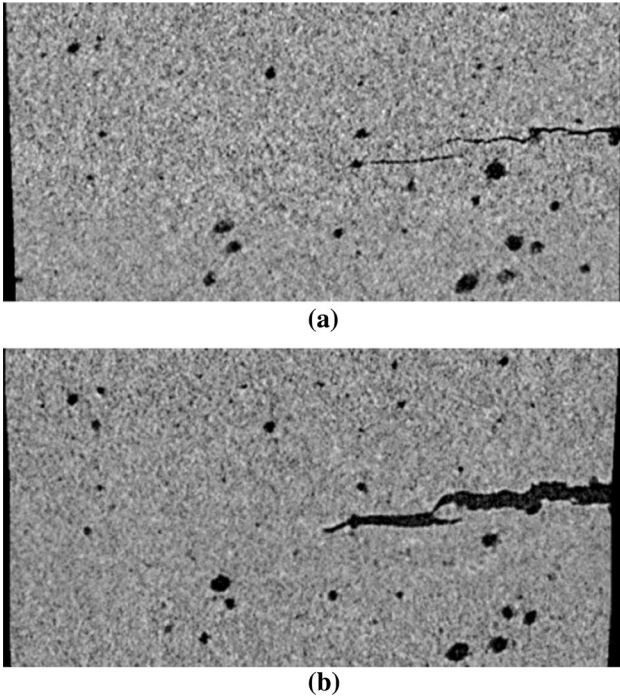

(a)

(b)

Fig. 14—The crack observation on cross section in longitudinal direction in specimen #1; (*a*) is XCT scanned in unloaded condition and (*b*) is XCT scanned in elastically loaded condition. Loading direction is vertical.
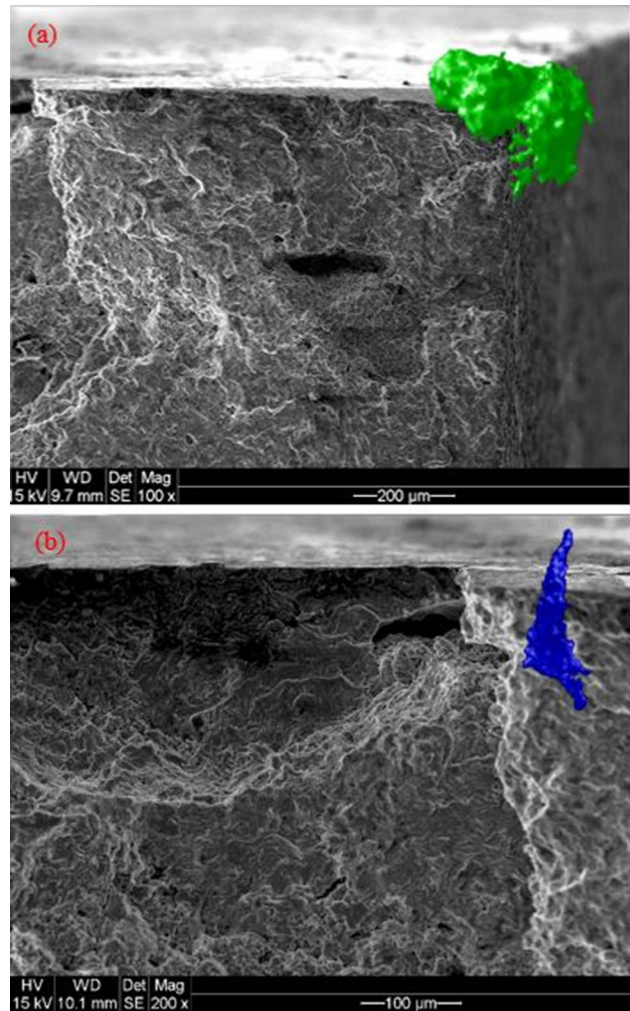

Fig. 16—Casting pores observed in SEM serving as crack initiation sites and the corresponding 3D geometry modeled using XCT data in specimen No. 2; (*a*) the crack initiation from pore No. 1 and (*b*) the crack initiation from pore No. 3. Loading direction is perpendicular to the fracture surfaces.
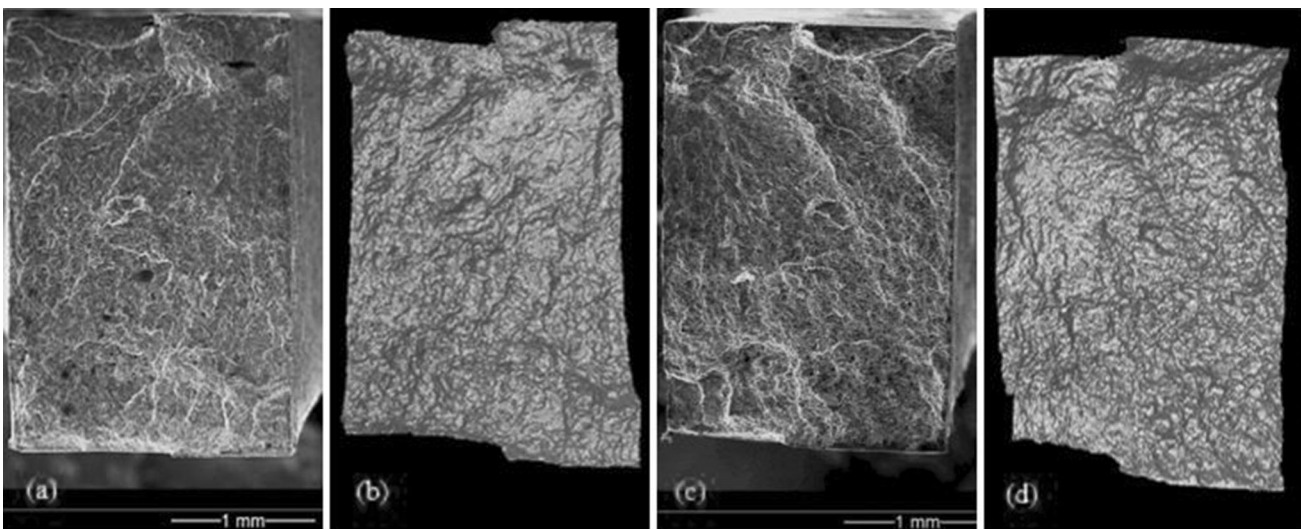

Fig. 15—Overall fracture surface from (*a*) SEM image of bottom part of specimen No. 2, (*b*) 3D model of the bottom part, (*c*) SEM image of the top part of specimen No. 2 and (*d*) 3D model of the top part. The loading direction is perpendicular to the cross-sectional views.

1. X-ray computed tomography is able to quantitatively characterize internal porosity in this alloy. Pores under 50 μm in volume-equivalent sphere diameter were found in the form of defect bands and larger pores were randomly distributed in the region between defect bands.
2. Pores were not found to grow during the fatigue test. Instead, a dominant fatigue crack was initiated either from large pores underneath the machined surface or from surface pores on the machined surface. A crack initiated from a pore underneath the casting surface was found to stop within the casting surface microstructure. During crack propagation, defect bands were observed to deflect the crack path. The crack presentation in the 3D model is less accurate in shape than 2D observation of cross sections due to crack closure effects. However, the 3D images provide important information about crack propagation direction and microstructure–crack interactions. Observing the crack by tomography is believed to better detect the crack initiation and propagation.
3. Applying a small amount of tension to the specimen while tomographic images are being captured is effective in removing the resolution issues just described.
4. X-ray tomography provides 3D accurate morphology of fracture surface that enables a better understanding of the crack initiation and crack–porosity interaction when interpreting SEM images in failure analysis.

REFERENCES

1. A.A. Luo: *J. Magnes. Alloy.*, 2013, vol. 1, pp. 2–22.
2. S. Mohd, Y. Mutoh, Y. Otsuka, Y. Miyashita, T. Koike, and T. Suzuki: *Eng. Fail. Anal.*, 2012, vol. 22, pp. 64–72.
3. L.H. Rettberg, J.B. Jordon, M.F. Horstemeyer, and J.W. Jones: *Metall. Mater. Trans. A*, 2012, vol. 43A, pp. 2260–74.
4. E. Maire and P.J. Withers: *Int. Mater. Rev.*, 2014, vol. 59, pp. 1–43.
5. J.-Y. Buffière, S. Savelli, P.H. Jouneau, E. Maire, and R. Fougères: *Mater. Sci. Eng. A*, 2001, vol. 316, pp. 115–26.
6. A. King, W. Ludwig, M. Herbig, J.-Y. Buffière, A.A. Khan, N. Stevens, and T.J. Marrow: *Acta Mater.*, 2011, vol. 59, pp. 6761–71.
7. W. Ludwig, J.-Y. Buffière, S. Savelli, and P. Cloetens: *Acta Mater.*, 2003, vol. 51, pp. 585–98.
8. T.J. Marrow, J.-Y. Buffiere, P.J. Withers, G. Johnson, and D. Engelberg: *Int. J. Fatigue*, 2004, vol. 26, pp. 717–25.
9. H. Toda, S. Masuda, R. Batres, M. Kobayashi, S. Aoyama, M. Onodera, R. Furusawa, K. Uesugi, A. Takeuchi, and Y. Suzuki: *Acta Mater.*, 2011, vol. 59, pp. 4990–98.
10. W. Elber: Ph.D. Thesis, University of New South Wales, Australia, 1968.
11. W. Elber: *Eng. Fract. Mech.*, 1970, vol. 2, pp. 37–44.